ADVANCED OPTICAL MATERIALS
www.advopticalmat.de

Fiber Bragg Gratings with Micro-Engineered Temperature Coefficients

*Zipei Song, Mohan Wang, Frank P. Payne, Patrick S. Salter, Tongyu Liu, Steve J. Elston, Martin J. Booth, Stephen M. Morris, and Julian A. J. Fells**

Fiber Bragg gratings (FBGs) are ubiquitous as sensors for a range of parameters and also as optical components in telecommunications systems. However, their temperature dependence of around +10 pm °C^{-1} is a limiting factor, making it challenging for sensors to discriminate strain from temperature, while telecommunications components require additional thermal stabilization. The temperature-dependent properties of optical fiber are micro-engineered by creating microchannels within the cladding using femtosecond laser-assisted etching. These channels are filled with low-loss refractive index liquids which have thermo-optic coefficients that are around 50 times greater magnitude than silica and the opposite sign. Low-loss FBGs are microfabricated in standard single-mode fiber, with wide control over their temperature coefficient between +10 and −55 pm °C^{-1}. A temperature-insensitive FBG is also fabricated which is stable to ±12.5 pm over a 17–45 °C range, which is an order of magnitude reduction in sensitivity. It has only ±3.5% reflectivity variation from the mean over this range and only 1.29 dB insertion loss.

1. Introduction

Fiber Bragg gratings (FBGs) are periodic or quasi-periodic structures written along an optical fiber that reflect light at wavelengths determined by their periodicity. They have been universally adopted as sensors for providing measurements of strain, temperature, pressure, and many other physical parameters in remote and inhospitable environments.[1] They are key components in telecommunications systems for dispersion compensation, filtering, and multiplexing. They are also used as reflectors for semiconductor and fiber lasers as well as for pulse compression and stretching, along with many other applications. However, a fundamental issue ever since their inception in 1977 has been their intrinsic temperature dependence.[2] While it is possible to use an athermal mechanical package design for FBG components,[3] such packages are unsuitable for sensors since the FBG is isolated from the surrounding environment, so alternative approaches are needed.

An important issue that has concerned the sensing community is the cross-sensitivity between strain and temperature.[2] The thermal change in the wavelength of reflected light is due to both thermal expansion and the dependence of the refractive index on temperature, while the strain response arises from both the physical extension and the photoelastic effect.[4] For a typical silica FBG sensor at 1550 nm, the temperature sensitivity is around 10–12 pm °C^{-1} and the strain sensitivity is ≈1.2 pm με^{-1}.[5,6] As a result, it is not possible to monitor either temperature or strain with a single measurement of an FBG. Discrimination between temperature and strain has attracted widespread attention and continuous attempts have been made over the last four and half decades.

Approaches such as using two wavelengths or using two polarization modes give only small changes in sensitivity.[7,8] A number of indirect approaches are known by combining an FBG with other types of optical fiber sensors. These include devices with multimode fibers,[9] using four-wave mixing,[10] with a Fabry–Pérot cavity,[11] with long-period gratings,[12] with a few-mode fiber,[13] with a no-core fiber,[14] with an erbium-doped fiber amplifier,[15] with a micro-structured fiber and with fiber polarization-rocking filters,[16,17] and many more. The magnitude of reflectivity can also provide information to solve the problem, such as analysis of sidelobe power and spectral analysis by machine learning.[18,19] However, intensity-based measurements are vulnerable to noise and bending losses. Alternative approaches include modification of the thermal or strain response of FBG sensors, which can then be compared with a conventional FBG sensor. Such modifications include strain compensation with a glass tube,[20] and altering the strain response with fibers of different diameters.[21,22] Fiber Bragg gratings have been written in tapered optical fiber to give a strain-induced bandwidth change,[23] but tapering the fiber compromises its mechanical strength. The temperature sensitivity of an FBG can be significantly enhanced by applying a coating with a high coefficient of thermal expansion to the FBG.[24] However, these devices rely on the thermal expansion of the coating to convert the

Z. Song, M. Wang, F. P. Payne, P. S. Salter, T. Liu, S. J. Elston, M. J. Booth, S. M. Morris, J. A. J. Fells
Department of Engineering Science
University of Oxford
Parks Road, Oxford OX1 3PJ, UK
E-mail: julian.fells@eng.ox.ac.uk

The ORCID identification number(s) for the author(s) of this article can be found under https://doi.org/10.1002/adom.202402726

DOI: 10.1002/adom.202402726

temperature change into a strain change of the fiber, hence they are not suitable for measuring other parameters such as strain. An FBG within a composite laminate was used to infer strain and temperature via induced birefringence,[25] but the additional materials make the fiber incompatible for embedding within infrastructure.

To directly change the temperature sensitivity of a waveguide, liquids, and polymers with negative temperature coefficients have been used. Silicon-on-insulator (SOI) waveguides have been made temperature-insensitive and highly temperature-sensitive by using polymer overlayers.[26–28] However, SOI waveguides have a very different material system with a high index contrast between the core and cladding, so the work does not translate to optical fibers that are weakly guiding. Bragg gratings within 5 µm diameter microfiber and fibers etched to within 0.3 µm of the core have been made temperature-insensitive by immersion in liquid.[29,30] The liquid has a large negative thermo-optic coefficient dn/dT to counter the positive coefficient of the silica. However, these devices are not suitable for sensing as the very thin fiber is not mechanically strong and it is impractical to have the fiber immersed in a liquid. They also appear to be multimoded.

There have been a number of reports of microstructured fiber with an array of holes in the cross-section that have been filled with a similar high negative dn/dT liquid. For example, Naeem et al. were able to achieve a modest change in temperature sensitivity using methanol-filled holes.[31] Alternatively, Huy et al. showed plots with flattened temperature response over a limited temperature range but did not show spectra for the filled fibers.[32] There is no information on loss and their best fiber appears to have a normalized frequency, $V > 2.4$ indicating it may be multi-moded. Recently, a fiber with a 2 µm hollow core was filled with a liquid to give a temperature sensitivity of −301 pm °C^{-1}.[33] However, the filled fiber appears to be lossy,[34] and the small mode field diameter would result in large splice losses to transmission fiber. It also appeared to show poor spectral performance and likely polarization dependence. Loss and spectral performance are critical parameters for FBG systems, particularly as multiple FBGs are often concatenated.

There have been theoretical papers proposing filled microstructured fibers for low - and high temperature sensitivity,[35–37] but these designs have not been realized experimentally. In this paper, we present a design framework for micro-engineering the temperature coefficients of FBGs over specified temperature ranges, while maintaining low loss and good spectral properties. We demonstrate this process by microfabrication of an FBG with a very large magnitude temperature coefficient and another that is temperature-insensitive.

2. Results

2.1. Analysis and Design

An FBG of uniform pitch reflects light predominantly at a wavelength known as the Bragg wavelength, λ_B, given by:[38]

$$m\lambda_B = 2n_{eff}\Lambda \tag{1}$$

where m is an integer representing the grating order, n_{eff} is the effective refractive index of the fiber and Λ is the pitch of the periodic structure. When there is a temperature or strain variation, both n_{eff} and Λ will vary accordingly. The shift in Bragg wavelength due to a change in temperature and strain is given by:[4]

$$\frac{\Delta\lambda_B}{\lambda_B} = \left(1 - \left(\frac{n_{eff}^2}{2}\right)\left[P_{12} - \nu\left(P_{11} + P_{12}\right)\right]\right)\epsilon + (\alpha + \xi)\,\Delta T \tag{2}$$

where $\Delta\lambda_B$ is the shift in Bragg wavelength due to the strain ϵ and temperature change ΔT, P_{ij} are the Pockel's coefficients of the stress-optic tensor, ν is Poisson's ratio, α is the linear thermal expansion coefficient and ξ is the thermal response of the fiber. The thermal response, ξ, is given by:

$$\xi = \frac{1}{n_{eff}}\frac{dn_{eff}}{dT} \tag{3}$$

In a conventional FBG, $\frac{dn_{eff}}{dT}$ is approximately equal to the thermo-optic coefficient of the fiber material (nominally $\frac{dn}{dT} = 7.97 \times 10^{-6}$ °C^{-1} for silica).[39] The Bragg wavelength shift due to an increase in temperature is positive across all temperature ranges. In order to design a device with a different thermal response, we need a material with a different thermo-optic coefficient. Refractive index liquids from Cargille Labs were selected for a much higher magnitude thermo-optic coefficient of $\frac{dn}{dT} = -395 \times 10^{-6}$ °C^{-1} with low loss.[40] Liquids with refractive indices between 1.420 to 1.460 at 1550 nm in 0.002 increments are available to be close to that of silica (1.444).[40]

The proposed FBG device configuration has microchannels filled with refractive index liquid in the cladding adjacent to the core as shown in **Figure 1a**. The dimensions of the microchannels and their proximity to the core vary according to the design. There is a Bragg grating within the fiber core. The four microchannels run along the length of the fiber in proximity to the core where the grating is located. There are advantages to having microchannels in the cladding as it allows a weaker interaction with the optical mode, thereby allowing greater design flexibility and lower loss. The channels are brought out to the side of the fiber so that capillary filling of the liquid is possible. As the temperature increases, the refractive index of the core, $n_{co,}$ and the cladding material, n_{cl} both increase, while the refractive index of the liquid, n_{liq}, decreases.

By engineering the waveguide design appropriately, we can adjust the temperature sensitivity and the operating temperature. In this work, we use two independent parameters to achieve this: i) The refractive index liquid proportion in the cladding (weighted to the overlap of the optical mode) and ii) the liquid refractive index at room temperature.

To analyze the device, we initially use the approximation that the microchannels around the core can be represented as a continuous band of material forming an inner cladding, as shown in Figure 1b. The amount of interaction with the optical mode and liquid region can be adjusted by varying the radius of the inner cladding. This approximation allows us to use the solution for a depressed cladding waveguide.[41,42] Although this solution was for waveguides where the inner cladding has a lower refractive

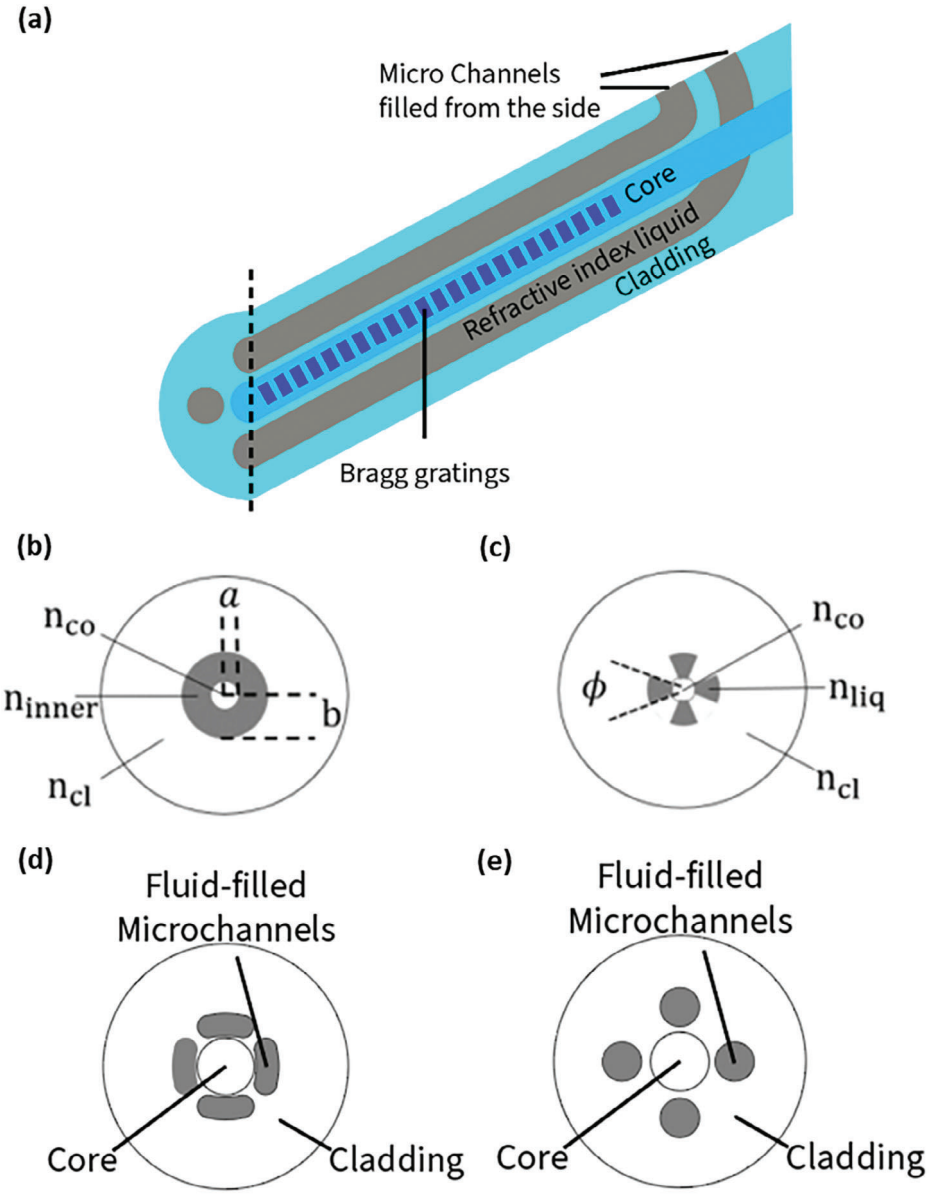

Figure 1. a) Device configuration (not to scale). b) Model of the fiber as a double cladding waveguide. c) Model of the fiber as a four-sector waveguide. The core has radius a and the inner cladding has radius b, and n_{co}, n_{cl}, n_{liq}, and n_{inner} are the refractive indices of the core, cladding, liquid, and inner cladding, respectively. d) Cross-section of the fabricated high-temperature sensitivity FBG. e) Cross-section of the fabricated temperature-insensitive FBG.

index than the outer material, it also holds true for cases where the inner cladding has a higher refractive index. The propagation constant β of a single-mode double-clad waveguide can be found from the following equation:[42]

$$\begin{aligned}&\left[\gamma J_0(\kappa a) I_1(\gamma a) + \kappa J_1(\kappa a) I_0(\gamma a)\right]\\&\times\left[\delta K_0(\gamma b) K_1(\delta b) - \gamma K_1(\gamma b) K_0(\delta b)\right]\\&+\left[\gamma J_0(\kappa a) K_1(\gamma a) - \kappa J_1(\kappa a) K_0(\gamma a)\right]\\&\times\left[\delta I_0(\gamma b) K_1(\delta b) + \gamma I_1(\gamma b) K_0(\delta b)\right] = 0\end{aligned} \tag{4}$$

where K_q, J_q, and I_q are the modified Hankel, Bessel, and modified Bessel functions of order q, a is the radius of the core and b is the radius of the inner cladding. The outer cladding is assumed to have an infinite radius. The terms in Equation 4 are defined for our case in Figure 1b as:

$$\kappa = \sqrt{n_{cl}^2(1+\Delta)^2 k^2 - \beta^2} \tag{5}$$

$$\gamma = \sqrt{\beta^2 - n_{cl}^2(1+\Delta')\,k^2} \tag{6}$$

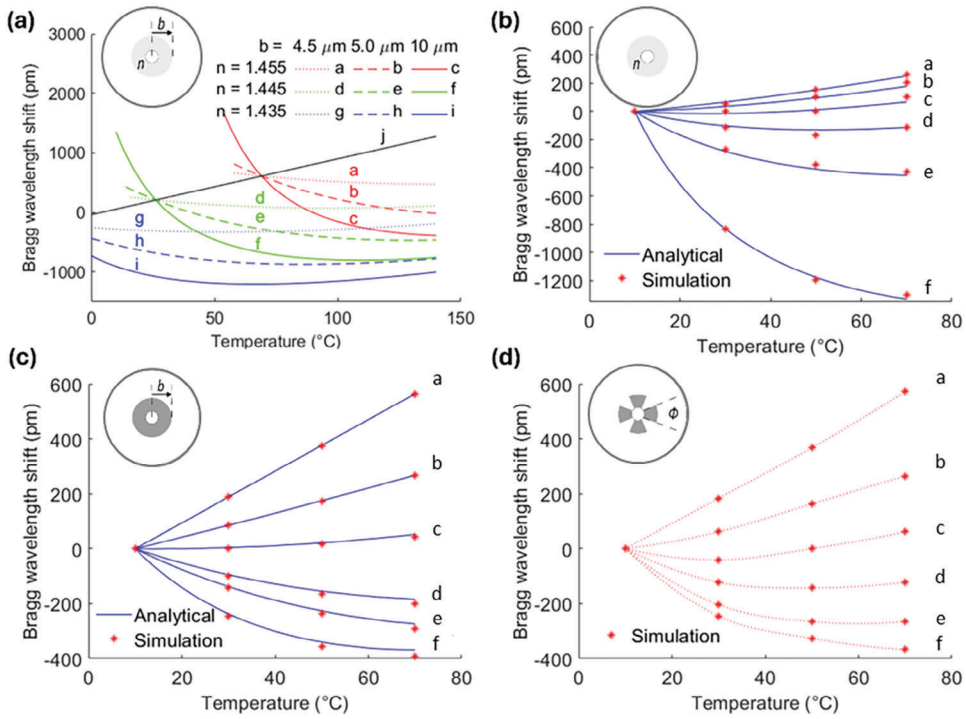

Figure 2. Modeling of the Bragg wavelength shifts with temperature. a) The analytic calculation for the model in Figure 1b where lines a to i are for different values of b and n_{inner}, and line j is for $n_{inner} = n_{clad}$, equivalent to a standard FBG. b) Analytic calculation (–) and simulation (*) for the model of Figure 1b with $b = 12$ µm and $n_{inner} = 1.42$ (line a) to 1.44 (line f) in equal steps along the arrow. c) Analytic calculation (–) and simulation (*) for the model of Figure 1b with $n_{inner} = 1.436$ and $b = 4.1$ (line a) to 10 µm (line f) in equal steps along the arrow. d) Simulation for the model of Figure 1c with $\phi = 0$ (line a) to 90° (line f) in equal steps along the arrow. See Supporting Information for the underlying data.

$$\delta = \sqrt{\beta^2 - n_{cl}^2 k^2} \tag{7}$$

$$\Delta = \left(n_{co} - n_{cl}\right) / n_{cl} \tag{8}$$

$$\Delta' = \left(n_{co} - n_{inner}\right) / n_{cl} \tag{9}$$

where n_{co}, n_{inner} and n_{cl} are refractive indices of the fiber core, inner cladding, and outer cladding, respectively, β is the propagation constant and k is the wavenumber. We solved Equation 4 numerically to obtain the effective refractive index, n_{eff}, using $n_{eff} = \frac{\beta}{k}$. The Bragg wavelength can then be estimated using Equation 1, since the pitch of the grating is known. We analyzed the full parameter space, with different inner cladding radii and refractive indices.

Figure 2a shows analytic calculations of the shift in Bragg wavelength for different values of liquid refractive index and inner cladding diameter. It shows how different temperature sensitivities and operating wavelengths can be obtained by varying the design parameters. A general trend is that at lower temperatures the temperature sensitivity is negative which becomes positive at higher temperatures. We can quantitatively analyze the effects of the two independent parameters on the Bragg wavelength. Varying the liquid refractive index causes a horizontal translation of the plot and can be used to control the working temperature of the device. In contrast, varying the inner cladding radius (proportion of the liquid) causes a tilting of the plot, thus determining the thermal sensitivity. This analysis provides useful information for designing a device with the desired temperature sensitivity and working temperature range.

The strategy of designing such a device is important and here we demonstrate a general method as follows. A liquid proportion is selected first to meet the required temperature sensitivity. Generally, a lower liquid proportion results in a more positive thermal response, and a larger liquid proportion results in a more negative thermal response. Then the refractive index of the liquid is tuned to set the operating temperature. In order to achieve optimized parameters for specific designs we performed numerical simulations of the fiber, which allowed arbitrary shaped microchannels. In addition to simulating the model in Figure 1b, we also simulated the structure in Figure 1c, which has 4 microchannels with cross-sections in the shape of individual sectors of a circle (excluding the core and a small margin around it). This enables the liquid proportion to be varied by varying the sector angles. We employed the FIMMWAVE (Photon Design Ltd.) mode solver software. The fiber used in the simulation was SMF28e+ with a core diameter of 8.2 µm and a cladding diameter of 125 µm.[43] A convergence test was undertaken to determine the optimum cladding boundary to be 50 µm to speed up the simulation. The core index, n_{co}, and the cladding index, n_{cl}, of the fiber are 1.451 and 1.445, respectively.[44] The axial length of the FBG and the microchannels were 6 mm. The pitches were slightly tuned so that all Bragg wavelengths were not far from 1550 nm.

Figure 2b shows simulation results and analytic calculations for the double cladding waveguide of Figure 1b with an inner cladding radius 12 µm and the liquid refractive index varying

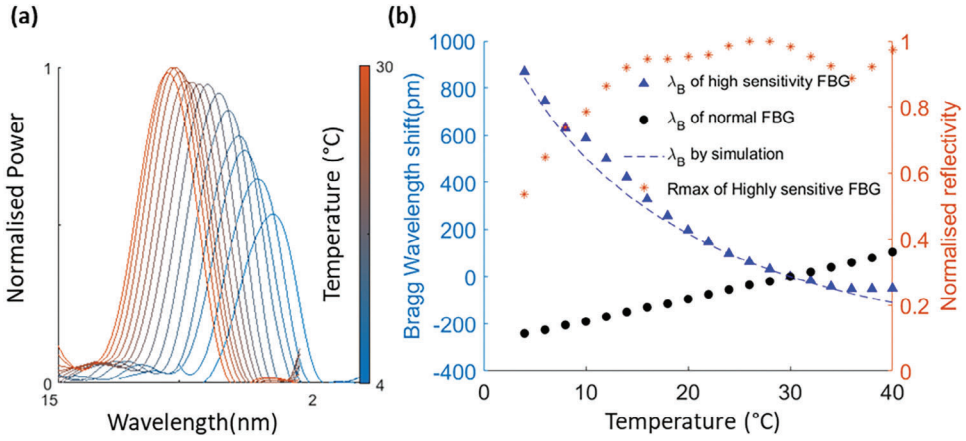

Figure 3. a) The experimentally measured reflection spectra at different temperatures from 4 to 30 °C in steps of 2 °C for a high-temperature sensitivity FBG device with a cross-section as per Figure 1d. b) Experimentally measured Bragg wavelength λ_B and peak reflectivity R_{max} against temperature for a high thermal sensitivity FBG device and a normal FBG for comparison. Also shown is the simulated change in Bragg wavelength. See Supporting Information for the underlying data.

between 1.42 and 1.44. Figure 2c shows simulation results and analytic calculations for the double cladding waveguide of Figure 1b with a liquid refractive index of 1.436 and the inner cladding radius varying between 4.1 and 10 μm. All the plots in Figure 2a–c show excellent consistency between the analytical calculations and the simulations. Figure 2d shows simulation results only for the four-sector waveguide of Figure 1c, where the sector angle Φ varies between 0° and 90°. Comparison of Figure 2c,d confirm that the thermal response of the FBG can be tuned in a similar way by either varying the inner cladding radius or varying the sector angle.

A general trend is that as the temperature increases, the thermal response of the Bragg wavelength increases (becomes more positive). This is because when n_{liq} is further away from n_{co} the impact of the liquid cladding is less significant than that of silica cladding. Eventually, at a higher temperature, the devices have a positive thermal response since the silica cladding dominates in the cladding region. In contrast, at a lower temperature where the liquid refractive index is higher, the liquid cladding dominates and the thermal response is therefore negative. A similar trend is seen from the liquid refractive index as shown in Figure 2b where the thermal response is more negative with a higher liquid refractive index (closer to the core index) and more positive with a lower liquid refractive index (further away from the core index). A different liquid proportion not only shifts the thermal response but also changes the range of the operating temperature. One extreme case is when the liquid proportion equals 100% where the device has a cladding made of liquid with the corresponding refractive index. In this case, the variation in thermal response due to temperature is high and can be approximated by a quadratic function. When the liquid proportion is zero, the device is a conventional FBG with a constant thermal response. Therefore, by varying the liquid proportion between the two extreme cases, we can set the required thermal sensitivity. Then by appropriate choice of liquid refractive index, we can shift the operating temperature window to match the required application.

2.2. A High-Temperature Sensitivity FBG

One motivation for this work is to fabricate a high-temperature sensitivity FBG device with low loss that could be used for temperature and strain discrimination. The highest sensitivity is obtained with the cladding formed entirely of liquid. However, a core surrounded entirely by fluid is mechanically unstable. So, some connections are left in between the liquid-filled channels as shown in Figure 1d. Each of the four channels is ≈7 μm × 10 μm in cross-section, arranged symmetrically leaving approximately a 0.5 μm gap between one another and close contact with the core. A relatively high liquid refractive index was chosen to be 1.440 at 1550 nm so that the operating temperature is at room temperature.

A tunable laser (Aglient 8164A) was used to measure the reflection spectra using an optical circulator and the built-in power meter. The high coherence source did result in a small amount of Fabry–Pérot ripple on the plots which was filtered out for clarity, while the raw data is provided in the Supporting Information. The measurement results are shown in **Figure 3**. The measured spectra of this device are plotted in Figure 3a over the working range of 4–30 °C. Figure 3b shows the peak Bragg wavelength and the peak reflectivity against temperature over a wider range of 4–40 °C. The bandwidth at different temperatures is approximately constant at 0.5 nm. The temperature sensitivity is the change in Bragg wavelength with temperature. The maximum temperature sensitivity is as large as −55 pm °C^{-1}. Over a temperature range of 4–20 °C, the average temperature sensitivity is −42 pm °C^{-1}. However, as the temperature increases, the sensitivity tends to reduce in magnitude and move to the positive side. Over the temperature range of 4–30 °C, the average temperature sensitivity within this range is −33pm °C^{-1}. Also plotted in Figure 3b are simulation results using the exact model of Figure 1d. The experimental results follow these simulation results closely.

The peak reflectivity, R_{max} is given by $R_{max} = \tanh^2(\kappa L_g)$ where κ is the coupling coefficient and L_g is the length of Bragg

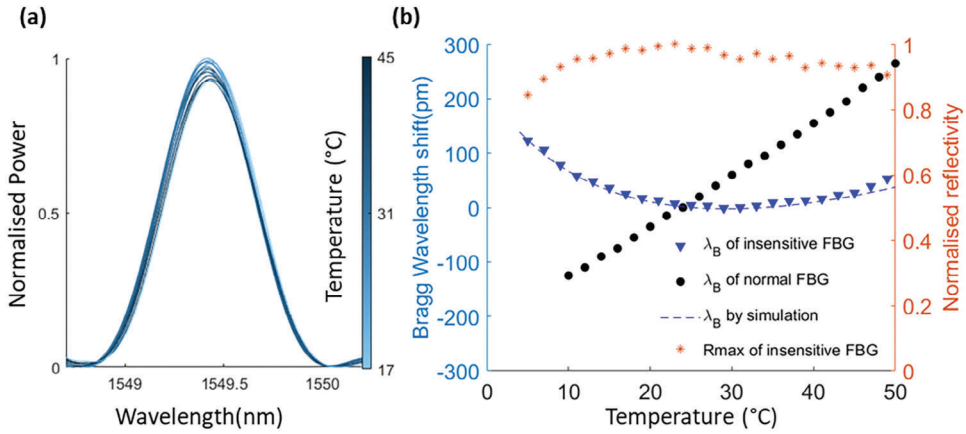

Figure 4. Experimental measurements on the temperature-insensitive FBG with a cross-section as per Figure 1e. a) Experimentally measured reflection spectra at different temperatures from 17 to 45 °C in steps of 2 °C. b) Experimentally measured Bragg wavelength λ_B and peak reflectivity R_{max} against temperature for the temperature-insensitive FBG, with a normal FBG for comparison. Also shown is the simulated change in Bragg wavelength. See Supporting Information for the underlying data.

grating. Although there are a few anomalous points at high temperatures, generally the reflectivity is lower at both high and low temperatures. At a lower temperature, the liquid refractive index is closer to the core index. The mode has expanded to the liquid region; thus, the coupling coefficient is lower. As a result, we expect a high-temperature sensitivity but a low peak reflectivity. This could be mitigated by writing the grating lines through a greater proportion of the core cross-section. As the temperature increases, the coupling coefficient gradually decreases, thus the temperature sensitivity decreases while the peak reflectivity increases. When the temperature increases further, the device will experience loss due to a mismatch in the cladding refractive index, resulting in coupling to radiative modes.

2.3. A Temperature-Insensitive FBG

An FBG with a compensated thermal response has also been designed and fabricated. The Bragg wavelength versus temperature response has a turning point. By operating near this turning point, the change in the Bragg wavelength with temperature can be minimized. In order to keep a low temperature-sensitivity near the turning point we reduced the liquid proportion in the evanescent field by moving the micro-channels further away from the core, as shown in Figure 1e.

The four channels are circular in shape with a diameter of ≈7 µm, leaving a larger gap of 1 µm away from the core to allow for some over-etch. The microchannels are fabricated with a high pulse energy of 0.290 µJ when the focal position is further away from the center, in order to overcome the aberration caused by the cylindrical fiber top surface. The liquid refractive index was chosen to be 1.432 at 1550 nm so that the device operates at room temperature with zero sensitivity centered at ≈30 °C.

Figure 4 shows measurements for the temperature-insensitive device. Figure 4a shows the reflectivity spectra for the FBG over a temperature range of 17–45 °C. These spectra show the device to be extremely temperature stable with only ±12.5 pm wavelength variation over this range, which is an 11-fold improvement over a conventional device. Furthermore, there is only ±3.5% reflectivity variation from the mean. These measurements show the device is very insensitive to temperature in terms of both reflectivity and wavelength. The bandwidth is also very constant at ≈0.5 nm. This is better than the high-sensitivity device since the modes are more confined within the core. The Bragg wavelength and peak reflectivity are shown in Figure 4b over a wider temperature range of 5–49 °C. This shows the device to be useable over a very wide temperature range, with only ±61.5 pm variation. We determined that there had been some over-etch, whereby the KOH removed some of the pristine silica. Also shown in Figure 4b are simulation results for the structure in Figure 1e, with a hole diameter of 8.16 µm instead of 7 µm to take into account this over-etch. These results show exceptional agreement between the simulation results and the experimental results.

Figure 5 shows the transmission spectrum and a microscope image of the temperature-insensitive device. To measure the insertion loss of the device, FC/APC pigtails were spliced to each end of the FBG, and the transmission spectrum was recorded, shown in Figure 5a at an input power of 0.71 mW. This gives a connector-to-connector insertion loss of 1.29 dB, meaning that the likely loss of the device is ≈1 dB. The FBG had a reflectivity of ≈10%. The polarization dependence of the Bragg wavelength was determined by varying the input polarization to find the maximum and minimum Bragg wavelengths at each temperature over the operating range. The largest difference in Bragg wavelength between the two orthogonal polarizations was found to be 17.4pm.

3. Discussion

It is clear from the plots in Figures 3,4 that we have tuned the temperature sensitivity to be either very high or very low, in a temperature range around room temperature. It is notable that a design with any desired temperature-sensitivity in between can also be fabricated. While a large temperature coefficient gives better sensitivity, it also requires more bandwidth for a given operating temperature range, thus reducing the number of sensors that may be multiplexed. Hence having the ability to adjust the sensitivity is a useful design parameter. Meanwhile, the spectra

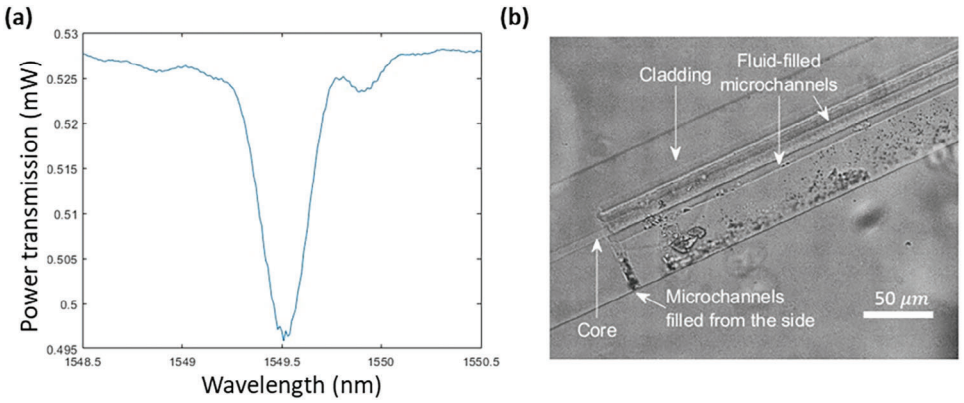

Figure 5. a) The transmission spectrum at room temperature for the temperature-insensitive FBG. The input power was measured to be 0.71 mW. See Supporting Information for the underlying data. b). A microscope image of the temperature-insensitive FBG device near one end of the microchannels.

remain single-mode with only one peak present. The loss was measured to be −1.29 dB so the devices are suitable for many practical applications. The main source for the losses is defects during the laser fabrication and etching processes which could potentially be improved with better manufacturing. As the device is made of standard fibers there should be no additional splicing and mode-mismatch losses between dissimilar fiber types. In principle, a custom fiber could be manufactured as an alternative to etching. In this case, the fiber with the FBG may be spliced to conventional fiber to minimize losses. The reflectivity is relatively stable for the high-sensitivity device and extremely stable for the temperature-insensitive device over their working temperatures. We initially used glycerol for the injected liquid, but we found that the loss at 1550 nm was high and there was a large variation in reflectivity with temperature. We have included this work in the Supporting Information since it may be of value, particularly for use at other wavelengths. Potentially, rather than room temperatures, the device could also be designed to have high or low temperature-sensitivity for elevated temperatures such as for monitoring lithium-ion batteries.

The applications for the high temperature-sensitivity device involve simultaneous strain and temperature measurements by using it in conjunction with a conventional FBG. Each measurement gives two comparable Bragg wavelengths λ_1 and λ_2 from each of the two sensors. Therefore, temperature and strain discrimination can be achieved by solving the matrix:

$$\begin{pmatrix} \Delta\lambda_1 \\ \Delta\lambda_2 \end{pmatrix} = \begin{pmatrix} K_{\{\epsilon 1\}} & K_{\{T1\}} \\ K_{\{\epsilon 2\}} & K_{\{T2\}} \end{pmatrix} \begin{pmatrix} \epsilon \\ \Delta T \end{pmatrix} \tag{10}$$

where K_{ij} are the sensitivities for strain ϵ and temperature change ΔT for the two FBGs. The high-sensitivity FBG device could also potentially be used in thermally tunable devices such as filters and add-drop multiplexers, where the reflected wavelength is determined by temperature.

The temperature-insensitive device, on the other hand, could be used for strain sensing with low temperature-cross-sensitivity, using only a single sensor per measurement. As a result, there is no reduction in multiplexing as the bandwidth per measurement is less than two sensors. Also, there are no additional complicated schemes required and the device can be simply a replacement for existing sensors. Another application is for passive temperature-stabilized components, such as optical filters, FBG stabilized lasers, and fiber lasers. Our temperature-insensitive FBG would further improve the wavelength tolerance of such devices. The temperature-insensitive devices would also find application wherever a stable reference is required, such as for spectroscopy, instrumentation, and optical fiber sensor interrogators.

The process is compatible with all step-index fibers, such as fiber for 980 nm pump lasers. Although we used uncoated fiber, it is also possible to use coated fiber. Potentially it may be possible to write the main structures through the coating and only breach the coating for access channels, or alternatively, the stripped coating may be re-coated. If the fiber has a coating then the thermal expansion of the coating may need to be considered in addition, thus transforming Equation (2) into:[45]

$$\frac{\Delta\lambda_B}{\lambda_B} = \left(1 - P_e\right) + \left[\left(1 - P_e\right)\alpha_c + \xi\right]\Delta T \tag{11}$$

where α_c is the thermal expansion coefficient of the fiber coating and P_e is the photo elastic coefficient given by $P_e = (\frac{n_{eff}^2}{2})\,[P_{12} - \nu(P_{11} + P_{12})]$. In this case $(1 - P_e)\alpha_c$ may dominate over ξ. However, the temperature dependence can be compensated if the fiber can be modified such that ξ is made approximately equal to $-(1 - P_e)$.

The manufacturing process allows the shapes of the microchannels to be arbitrary in three dimensions. It therefore allows tapering of the transition between the fiber with the microchannels to minimize mode loss. The technique is not limited to the material used in these examples. For a commercial device, the entry and exit holes would need to be sealed, which could potentially be achieved by selective laser melting with a focused high-power laser. Rather than use the refractive index oils, UV-curable polymer resins used, which would avoid the need to seal in the liquid. Potentially, a similar process can be used to fabricate fiber devices with active materials such as liquid crystal materials. There is also the possibility of having further microchannels within the fiber for incorporating electrodes to form electrically tunable devices. A preliminary account of the experimental results was presented at the Optical Fiber Sensors Conference.[46]

4. Conclusion

To conclude, we have demonstrated FBG devices with micro-engineered temperature sensitivities. The devices were fabricated by laser inscription followed by chemical etching to allow refractive index liquid to be inserted into the cladding of commercial optical fibers. A device with a large temperature-sensitivity has been fabricated and measured to have a near second-order response of up to −55 pm °C^{-1} near 4 °C. It has an average temperature sensitivity of −33 pm °C^{-1} over the range of 4–30 °C, with low variation in reflectivity. The device could be used to produce a large thermal sensitivity compared with a conventional silica FBG sensor to achieve strain and temperature discrimination. Another device has shown an exceptionally low-temperature variation of ±12.5 pm over a temperature range of 17–45 °C. The device has only 1.29 dB loss and the reflectivity variation with temperature is only ±3.5% from the mean. This temperature sensitivity is over an order of magnitude less than conventional FBGs over this range. This device will potentially provide a large improvement in FBG laser stabilization. It may become an enabling technology for strain sensing with low temperature-cross-sensitivity using existing sensor interrogation systems. It also has applications where tightly controlled wavelength references are required.

The flexible design process allows the temperature sensitivity to be adjusted between +10 and −55 pm °C^{-1} and the center of the temperature range to be adjusted within the limits of the infiltrated material. This enables the needs of a wide range of optical devices and optical fiber sensing applications to be met. Furthermore, there is the potential for new classes of tunable optical devices using this fabrication platform.

5. Experimental Section

The microchannels in this work were formed by laser writing in the fiber followed by a selective etch to remove the material in the exposed regions. A regenerative femtosecond laser system (Light Conversion Pharos SP-06-1000-PP) was used at a second harmonic generation wavelength of 515 nm and a pulse duration of 170 fs. A half-waveplate in conjunction with a polarizer was used to control the pulse energy between 10 and 300 nJ. A spatial light modulator (SLM) (Hamamatsu X10468) was used to compensate for the aberration generated in the optical path of the whole system. The fiber was taped onto a microscope slide and placed on a motion stage (*x*, *y*: Aerotech ABL10100L and *z*: ANT95-3-V). The positional accuracy of the stage was <10 nm for *x*, *y*, and *z*. The objective used had a ×20 magnification and numerical aperture of 0.5. A second-order FBG was written in standard single-mode fused silica fiber (SMF28e+ equivalent, Leader Optec Ltd.) by scanning the laser focus along the center of the fiber core. The FBG was written with a pulse energy of 0.15 µJ and a repetition rate of 100 Hz, controlled by a pulse picker. The writing speed was 0.1071 mm^{-1}s^{-1} so after the strain induced by the fiber mounting was relieved, the Bragg wavelength was ≈1550 nm. The errors in the fabricated gratings were ±0.01 µm.

The microchannels were written in the fiber with a pulse energy of between 0.26 and 0.29 µJ at a repetition rate of 250 kHz and a speed of 0.1 mm^{-1}s^{-1}, with the polarization perpendicular to the writing direction. These microchannels were written alongside the core, with access points to the fiber surface to enable filling. The devices were fabricated without immersion oil, thus aberration correction for the fiber surface in the air was required.[47] The Bragg gratings were 3 mm long and the channels were also 3 mm long with each having three access points, one at each end and one in the middle. The fiber was then placed in 8 mol L^{-1} KOH solution and etched for ≈13–17 h at 60 °C on a hotplate in a water bath, to preferentially remove the laser-exposed microchannel regions. The selectivity of etching is up to 300 and the error in microchannel diameter is ± 0.2 µm. Finally, the etched microchannels were filled with refractive index liquid by capillary action. The top view of a micro-fabricated FBG device is shown in Figure 5b. A number of devices were fabricated during the course of this work and experimental results from these are summarized in the Supporting Information.

Supporting Information

Supporting Information is available from the Wiley Online Library or from the author.

Acknowledgements

This work was supported by the UK Engineering and Physical Sciences Research Council (EP/T00326X/1).

Conflict of Interest

The authors declare no conflict of interest.

Author Contributions

Z.S., P.S., T.L. performed Waveguide and aberration simulations. Z.S., M.W., P.S. conducted Device fabrication and experimental measurements. Z.S., F.P.P., J.A.J.F. carried out theoretical work. Z.S., F.P.P., J.A.J.F. handled data analysis. Z.S., S.M.M., F.P.P., J.A.J.F. did manuscript preparation. J.A.J.F. led conceptual development. Project Supervision was provided by S.J.E., M.J.B., S.M.M., and J.A.J.F.

Data Availability Statement

Data underlying the results presented in this paper are provided in the Supporting Information.[48]

Keywords

fiber Bragg gratings, microchannel fibers, optical waveguides, temperature compensation, ultrasensitive

Received: October 9, 2024
Revised: December 15, 2024
Published online: January 16, 2025

[1] S. J. Mihailov, *Sensors* **2020**, *12*, 1898.
[2] K. O. Hill, Y. Fujii, D. C. Johnson, B. S. Kawasaki, *Appl. Phys. Lett.* **1978**, *32*, 647.
[3] Y. Huang, J. Li, G. Kai, S. Yuan, X. Dong, *Microw. Opt. Technol. Lett.* **2003**, *39*, 70.
[4] A. D. Kersey, M. A. Davis, H. J. Patrick, M. LeBlanc, K. P. Koo, C. G. Askins, M. A. Putnam, E. J. Friebele, *J. Lightwave Technol.* **1997**, *15*, 1442.
[5] B.-O. Guan, H.-Y. Tam, X.-M. Tao, X.-Y. Dong, *IEEE Photonics Technol. Lett.* **2000**, *12*, 675.
[6] Y. J. Rao, A. B. L. Ribeiro, D. A. Jackson, L. Zhang, I. Bennion, *Opt. Lett.* **1995**, *20*, 2149.

[7] M. G. Xu, J.-L. Archambault, L. Reekie, J. P. Dakin, *Electron. Lett.* **1994**, *30*, 1085.
[8] G. Chen, L. Liu, H. Jia, J. Yu, L. Xu, W. Wang, *IEEE Photon. Technol. Lett.* **2004**, *16*, 221.
[9] D.-P. Zhou, L. Wei, W.-K. Liu, Y. Liu, J. W. Y. Lit, *Appl. Opt.* **2008**, *47*, 1668.
[10] C. Ghosh, V. Priye, *IEEE Sensors J.* **2020**, *20*, 14181.
[11] W.-C. Du, X.-M. Tao, H.-Y. Tam, *IEEE Photonics Technol. Lett.* **1999**, *11*, 105.
[12] H. J. Patrick, G. M. Williams, A. D. Kersey, J. R. Pedrazzani, A. M. Vengsarkar, *IEEE Photonics Technol. Lett.* **1996**, *8*, 1223.
[13] X. Gao, T. Ning, C. Zhang, J. Xu, J. Zheng, H. Lin, J. Li, L. Pei, H. You, *Opt. Commun.* **2020**, *454*, 124441.
[14] C. Li, T. Ning, X. Wen, J. Li, J. Zheng, H. You, H. Chen, C. Zhang, W. Jian, *Opt. Commun.* **2015**, *343*, 6.
[15] J. Jung, H. Nam, J. H. Lee, N. Park, B. Lee, *Appl. Opt.* **1999**, *38*, 2749.
[16] O. Frazao, J. P. Carvalho, L. A. Ferreira, F. M. Araújo, J. L. Santos, *Meas. Sci. Technol.* **2005**, *16*, 2109.
[17] S. E. Kanellopoulos, V. A. Handerek, A. J. Rogers, *Opt. Lett.* **1995**, *20*, 333.
[18] S. Sarkar, M. Tarhani, M. Khosravi Eghbal, M. Shadaram, *J. Appl. Phys.* **2020**, *127*, 114503.
[19] S. Sarkar, D. Inupakutika, M. Banerjee, M. Tarhani, M. Shadaram, *IEEE Photonics Technol. Lett.* **2021**, *33*, 876.
[20] M. Song, S. B. Lee, S. S. Choi, B. Lee, *Opt. Fiber Technol.* **1997**, *3*, 194.
[21] S. W. James, M. L. Dockney, R. P. Tatam, *Electron. Lett.* **1996**, *32*, 1133.
[22] X. Li, D. Wang, F. Zhao, E. Dai, *Microw. Opt. Technol. Lett.* **2004**, *43*, 478.
[23] H. F. Lima, P. F. Antunes, J. de Lemos Pinto, R. N. Nogueira, *IEEE Sensors J.* **2009**, *10*, 269.
[24] V. Mishra, M. Lohar, A. Amphawan, *Optik* **2016**, *127*, 825.
[25] A. K. Singh, S. Berggren, Y. Zhu, M. Han, H. Huang, *Smart Mater. Struct.* **2017**, *26*, 115025.
[26] W. N. Ye, J. Michel, L. C. Kimerling, *IEEE Photonics Technol. Lett.* **2008**, *20*, 885.
[27] M. M. Milošević, N. G. Emerson, F. Y. Gardes, X. Chen, A. A. D. T. Adikaari, G. Z. Mashanovich, *Opt. Lett.* **2011**, *36*, 4659.
[28] S.-L. Tsao, P.-C Peng, *Microw. Opt. Technol. Lett.* **2001**, *30*, 321.
[29] S. Gao, L. Jin, Y. Ran, Li-P Sun, J. Li, B-Ou Guan, *Opt. Express* **2012**, *20*, 18281.
[30] K. T. Kim, I. S. Kim, C.-H. Lee, J. Lee, *Sensors* **2012**, *12*, 7886.
[31] K. Naeem, Y. Chung, presented at *OECC and Australian Conference on Optical Fibre Technology*, IEEE, Piscataway, NJ, USA **2014**, 795.
[32] M. C. P. Huy, G. Laffont, V. Dewynter, P. Ferdinand, D. Pagnoux, B. Dussardier, W. Blanc, *IEEE Sensors J.* **2008**, *8*, 1073.
[33] W. Cheng, S. Liu, S. Zhao, L. Li, *Opt. Lett.* **2023**, *48*, 3941.
[34] L. Chen, Q. Su, S. Liu, L. Li, *Optik* **2021**, *243*, 167336.
[35] N. Mothe, D. Pagnoux, M. C. P. Huy, V. Dewinter, G. Laffont, P. Ferdinand, *Opt. Exp.* **2008**, *16*, 19018.
[36] W. Man, C. Zhang, J. Huang, Q. He, *Opt. Eng.* **2019**, *58*, 116101
[37] W. Man, J. Feng, J. Peng, *Opt. Eng.* **2012**, *51*, 085004.
[38] W. W. Morey, G. Meltz, W. H. Glenn, *SpIE* **1990**, *1169*, 98.
[39] D. B. Leviton, B. J. Frey, *SpIE* **2006**, *6273*, 800.
[40] Cargille labs, *Refractive-Index-Liquid-Series-AA-n-1.4400-at-589.3-nm-and-25 °C*, Cargille Labs, Cedar Grove, NJ, USA **2018**.
[41] L. G. Cohen, D. Marcuse, W. L. Mammel, *IEEE Trans. Microw. Theory Tech.* **1982**, *30*, 1455.
[42] S. Kawakami, S. Nishida, *IEEE J. Quant. Electron.* **1974**, *10*, 879.
[43] Corning, *Corning ® SMF-28e+ ® Photonic Optical Fiber*, Corning, Glendale, AZ, USA **2010**.
[44] Q. Wu, Y. Semenova, P. Wang, G. Farrell, *J. Opt.* **2011**, *13*, 125401.
[45] D. Sengupta, M. S. Shankar, P. S. Reddy, R. L. N. S. Prasad, K. S. Narayana, P. Kishore, *SpIE* **2011**, *8311*, 831103.
[46] Z. Song, M. Wang, P. S. Salter, T. Liu, S. J. Elston, M. J. Booth, S. M. Morris, J. A. J. Fells, in *28th Int. Conf. on Optical Fiber Sensors*, Optica Publishing Group, Naka-ku, Hamamatsu-shi, Japan, **2023**, W2.2.
[47] P. S. Salter, M. J. Woolley, S. M. Morris, M. J. Booth, J. A. J. Fells, *Opt. Lett.* **2018**, *43*, 5993.
[48] Z. Song, M. Wang, F. P. Payne, P. S. Salter, T. Liu, S. J. Elston, M. J. Booth, S. M. Morris, J. A. J. Fells Dataset1 Fiber Bragg gratings with micro-engineered temperature coefficients [Data set]. University of Oxford. **2025**, https://doi.org/10.5287/ORA-B7XAMR97Y.